Cross sections for ionization of tetrahydrofuran by protons at energies between 300 and 3000 keV

Mingjie Wang,[1,*] Benedikt Rudek,[1] Daniel Bennett,[1] Pablo de Vera,[2] Marion Bug,[1] Ticia Buhr,[1] Woon Yong Baek,[1] Gerhard Hilgers,[1] and Hans Rabus[1]

[1]*Physikalisch-Technische Bundesanstalt, Bundesallee 100, 38116 Braunschweig, Germany*

[2]*Department of Physical Sciences, The Open University, Walton Hall, MK7 6AA Milton Keynes, United Kingdom*

(Received 24 February 2016; revised manuscript received 11 April 2016; published 20 May 2016)

Double-differential cross sections for ionization of tetrahydrofuran by protons with energies from 300 to 3000 keV were measured at the Physikalisch-Technische Bundesanstalt ion accelerator facility. The electrons emitted at angles between 15° and 150° relative to the ion-beam direction were detected with an electrostatic hemispherical electron spectrometer. Single-differential and total ionization cross sections have been derived by integration. The experimental results are compared to the semiempirical Hansen-Kocbach-Stolterfoht model as well as to the recently reported method based on the dielectric formalism. The comparison to the latter showed good agreement with experimental data in a broad range of emission angles and energies of secondary electrons. The scaling property of ionization cross sections for tetrahydrofuran was also investigated. Compared to molecules of different size, the ionization cross sections of tetrahydrofuran were found to scale with the number of valence electrons at large impact parameters.

DOI: 10.1103/PhysRevA.93.052711

I. INTRODUCTION

Ionization of neutral atoms and molecules by charged particle impacts has been subject to extensive investigations for decades. The ionization processes as well as total, single-differential, and double-differential ionization cross sections for diverse targets have been summarized in several reviews [1–4]. Recently, cross sections were reported from the fully differential measurements [5] for simple targets such as helium [6–8] as well as for molecular hydrogen [9]. Since direct ionization by the primary ions and subsequent cascades of ionizations produced by the secondary electrons play the decisive role in ion-induced radiation damage of biological materials [10,11], further studies of ionization cross sections have been devoted to several complex molecules.

Since water molecules are commonly used as a default medium to describe living tissue, the ionization cross sections of water by proton impact have been experimentally investigated in the past [12–15]. On the other hand, theoretical studies of fully, double-, and single-differential and total ionization cross sections have also been extensively performed [16–18]. While there is a significant amount of literature on water molecules, only a few experimental data have been published recently for those of complex biological molecules like DNA or RNA constituents. Tabet *et al.* [19] presented the total ionization cross sections (TICS) of nucleobases (adenine, cytosine, thymine, and uracil) at proton energies below 150 keV. Iriki *et al.* [20,21] and Itoh *et al.* [22] reported the data of uracil and adenine for proton energies of 0.5, 1, and 2 MeV. Theoretically, Champion *et al.* [23] obtained double-differential ionization cross sections (DDCS), single-differential cross sections (SDCS), and TICS for ionization of different nucleobases by means of the first Born approximation with Coulomb wave (FBA-CW) model. Furthermore, a semiempirical model based on the dielectric formalism was developed by de Vera *et al.* [24,25] for the ion-impact ionization of biomaterials.

According to the data of Iriki *et al.* [20] for 1 MeV protons, the angular distributions of secondary electrons for adenine deviate significantly from those for simple targets, i.e., molecular hydrogen at emission angles smaller and larger than the binary encounter peak. These discrepancies are due to the differences in momentum distribution of respective target electrons. Along this line, Iriki *et al.* [20] found better agreement when comparing the adenine distributions to those of different hydrocarbon molecules, as their momentum distributions are more alike. Still for 1 MeV protons, the angular distribution of secondary electrons are slightly broader for adenine compared to those of hydrocarbons, and large discrepancies are expected for protons of lower velocities due to a large contribution of two-center effects [4]. Disagreements between adenine data of 1 MeV [20] and the calculation of de Vera *et al.* [25] are also found at emission angles outside the range of the binary encounter peak. To better understand the origin of those discrepancies, an extended comparison to other complex targets and also to lower proton energies is strongly required. However, to our best knowledge, reliable experimental cross-section data for biological molecules are still largely lacking.

As the presented studies of ionization for complex biomolecules cover only the DNA or RNA nucleobases, we report proton-impact measurements on tetrahydrofuran (THF, C_4H_8O), which is used for modeling the deoxyribose group in the sugar-phosphate backbone of DNA. This experimental determination was performed using a double-differential measurement, which provides a detailed description of both energy and angular distributions of emitted electrons. The information from fully differential measurements would complete the knowledge of the ionization process, but for such a massive target, the recoil-ion momentum would be hardly resolvable [26,27] and is not required due to the negligible contribution to the total radiation damage.

The interaction cross sections presented in the current paper are the DDCS, SDCS, and TICS for ionization of THF impacted by protons with energies between 300 and 3000 keV. The protons of these energies are relevant to ion-beam cancer

*mingjie.wang@ptb.de

therapy, which has become a standard technique for certain tumor types, in particular for tumors close to critical organs at risk. It is superior in its remarkable ballistic precision and biological effectiveness, which is due to the sharp and narrow maximum in the depth-dose curve at the end of the ion trajectories, the so-called Bragg peak [28–30], where a large amount of energy is deposited in densely spaced ionizations by protons with energies on the order of those selected in this work.

This paper is organized as follows. In Sec. II the experimental method and instrumentation are described. The data analysis is presented in Sec. III. The theoretical models are briefly introduced in Sec. IV. The experimental results are reported in Sec. V and are compared to the theoretical calculations. Differences from well-known cross sections of smaller targets, e.g., hydrogen, water, and hydrocarbon molecules, are also discussed. Finally, a conclusion is given in Sec. VI.

II. EXPERIMENT

The measurements were carried out using a crossed-beam arrangement where the primary ion beam was perpendicular to an effusive gas jet target of THF in a high-vacuum chamber. Inside this scattering chamber a hemispherical electron analyzer was mounted on a turntable such that the spectrometer could be rotated around the axis of the gas jet. Electrons ejected from the interaction zone could thus be detected and analyzed with respect to their energy and emission angle.

A. Apparatus

The proton beam was generated by a 3.75 MV Van de Graaf accelerator [31]. The proton energies were 300, 420, 840, 1200, 1550, 2000, and 3000 keV. The accuracy of the ion energy was ±1 keV [32]. A differential pumping stage was inserted as a buffer unit to prevent leakage of target gas into the high vacuum of the beamline. Inside, three tantalum apertures with diameters of 5, 3, and 5 mm were used to collimate the beam. The current on the inner aperture was recorded by an electrometer to detect possible changes of the beam position. The outer apertures were biased to −300 V in order to suppress electron emissions from the middle aperture such that only the direct current of protons hitting the middle aperture was recorded. A Faraday cup with an entrance aperture of 15 mm was placed on the far side of the scattering chamber in order to measure the beam current. Mechanical alignment of the Faraday cup, the apertures, and the rotation axis of the spectrometer was carried out using an optical telescope. The proton beam was aligned by maximizing the ratio of the current in the Faraday cup to the current on the central aperture. When optimally aligned, the current in the Faraday cup was on the order of 10^{-6} A, while the current onto the beam-confining aperture was on the order of from 10^{-8} to 10^{-7} A. The measured bias current on the Faraday cup in the absence of a beam was below 10^{-12} A.

Three orthogonal pairs of square-shaped Helmholtz coils [33] surrounding the scattering chamber were set up for compensation of the external magnetic fields. The dimensions of the three pairs were 90.5, 94.0, and 97.5 cm, respectively. Additionally, a mu-metal foil sheet was placed between the top of the turntable and the electron spectrometer to shield against

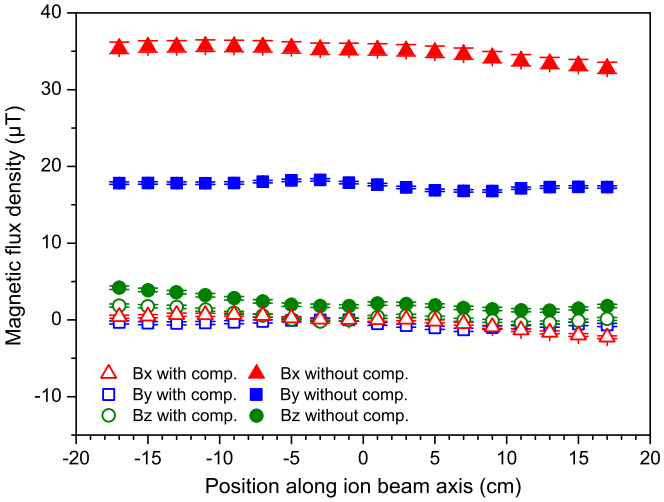

FIG. 1. Variation of the magnetic field along the beam axis with (open symbols) and without (solid symbols) compensation. Bx (red triangles), Bz (green dots), and By (blue squares) represent the orthogonal components of the magnetic field in the effusive gas jet direction, in the ion-beam direction, and in the direction perpendicular to the beam and gas jet, respectively.

the local magnetic field arising due to the iron-containing bearing of the rotation stage. Figure 1 shows the variation of the magnetic field along the beam axis with and without compensation. As a result, the residual magnetic field inside the scattering chamber was below 2.0 μT in a region of about 30 cm in diameter.

The effusive gas jet was produced through a tube terminated by a nozzle with an aperture of 0.3 mm in diameter. The tube was aligned along the rotation axis of the spectrometer. A three-axis micrometer manipulator was used to adjust the nozzle position with a precision of 0.01 mm. The distance between the tip of the nozzle and the axis of the primary beam was typically set to about 2 mm. For the production of the gas jet, a container filled with liquid THF of 99% purity was used as the vapor source. The vapor pressure of THF at 20° C is 173 mbar. Using a leak valve, the pressure of the THF gas at the entrance of the cylindrical tube was adjusted to 1 mbar. As a result, the base pressure in the scattering chamber rose from 10^{-7} mbar to the order of 10^{-5} mbar. The number density in the interaction zone, estimated using the formula given by Seccombe *et al.* [34], amounted to 1.3×10^{14} cm^{-3}. For the impact of a 100 eV electron, the total scattering cross section of THF is 29.13×10^{-16} cm^2 [35], giving a mean free path of about 26 mm, which is 26 times larger than the interaction zone length of 1 mm. This means that the single-collision conditions are fulfilled.

An AR 65 electron spectrometer purchased from Omicron Nanotechnology GmbH was used to detect the secondary electrons. It comprises an electrostatic input lens system, a hemispherical energy analyzer [36] with a mean radius of 65 mm, and channel electron multipliers. The secondary electrons entering the spectrometer are focused by the electrostatic lens system located at a distance of 29 mm from the interaction zone. The circular entrance aperture of the lens stack is 1 mm in diameter. The electrons passing through the analyzer are

detected by three channel electron multipliers behind the exit slits of the hemispherical condenser. The energy dispersions for each channel electron multiplier arising due to their different positions are corrected individually by configuration of the data acquisition software with the calibration values measured by the manufacturer. The spectrometer was operated in the constant-retard-ratio (CRR) mode, where the ratio of electron kinetic energy to analyzer pass energy is kept constant. The chosen value of CRR was 1 for the electron kinetic-energy range from 10 to 200 eV. Electrons of higher kinetic energies were analyzed with larger CRR values. The transmission of the analyzer decreases with increasing CRR value. Therefore, the count rates in the energy spectra between 200 and 400 eV (CRR 2), 400 and 600 eV (CRR 3) and 600 and 800 eV (CRR 4) were scaled up according to the CRR values used in order to compensate the decrease of the transmission.

B. Characterization of the spectrometer

Characterization of the spectrometer was done by means of the measurements using high-purity argon ($\geqslant 99.999\%$) as the reference gas. When the gas jet was operated with argon, the pressure inside the scattering chamber was also kept on the same order (10^{-5} mbar) as in the case of THF gas jet. The energy resolution of the spectrometer was determined by measuring the argon Auger spectrum produced by the impact of 1550 keV protons. The electrons emitted at 90° in the energy interval between 200 and 210 eV in steps of 0.1 eV were recorded. These measurements were made with CRR 2, resulting in a pass energy of argon Auger electrons of about 100 eV.

The measured $L_{2,3}M_{2,3}M_{2,3}$ Auger spectrum of argon is shown in Fig. 2. Peak 1 is chosen to determine the energy resolution of the spectrometer since this peak is known as a singlet without interfering satellite transitions. A value of 1 eV for the FWHM is obtained. This observed peak width results from several contributing linewidths, i.e., the natural line width, the instrumental resolution, and the width arising due to thermal Doppler broadening [37]. The contributions from the natural width (0.1 eV) [38] of the argon $L_{2,3}M_{2,3}M_{2,3}$ Auger lines and from the estimated width of thermal Doppler broadening (< 0.1 eV) [37] are small compared with the observed 1 eV FWHM and are therefore negligible. Hence, the instrumental energy resolution of the spectrometer was estimated to be 1 eV. Due to this limited energy resolution, the measured peaks 2 and 3 are each composed of two overlying Auger lines, which were resolved separately in the measurements reported by Mehlhorn and Stalherm [39]. In order to represent individual Auger lines, the measured spectrum is fitted by a superposition of six Gaussians with FWHM of 1 eV. The energy positions of those Gaussians are in good agreement with the literature data given in [39]. This also means that the energy calibration of the electron spectrometer is accurate within the uncertainty of 1 eV.

The accuracy of the angular positioning was checked by means of the differential elastic scattering cross sections of argon for 100 eV electrons. In this case, an electron gun with an energy width of ~0.6 eV was mounted at the entrance of the spectrometer chamber, and the electron beam was aligned by maximizing the current on the Faraday cup located on the opposite side of the spectrometer chamber. The angle of acceptance amounted to 2°, as the energy analyzer was equipped with an entrance aperture of 1 mm in diameter at a working distance of 29 mm. As Fig. 3 shows, a sharp minimum was predicted at the scattering angle around 123° in the theoretical calculations [40] from NIST, whereas the position of the minimum exhibited in our measurements agrees with that of literature data [40] within the angular resolution mentioned above.

C. Measurements

The energy spectra of the secondary electrons were measured from 10 to 800 eV at different detection angles θ. The

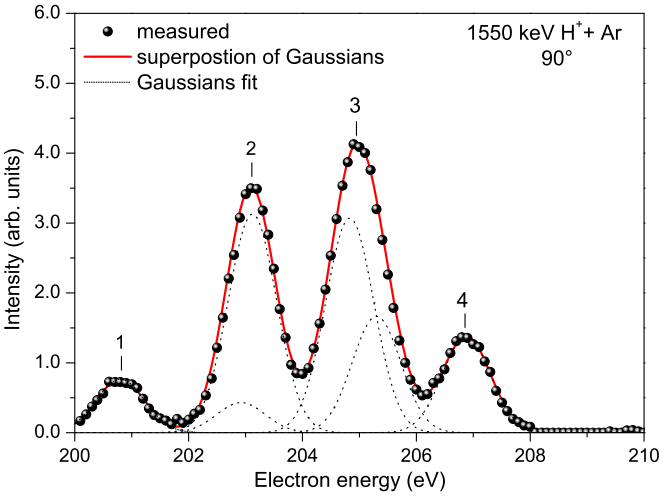

FIG. 2. $L_{2,3}M_{2,3}M_{2,3}$ Auger spectrum (symbols) of argon measured at 90° by 1550 keV protons. The peaks are numbered arbitrarily for identification. The measured spectrum is fitted by the superposition (solid line) of Gaussians (dashed lines) with a FWHM of an estimated energy resolution of 1 eV.

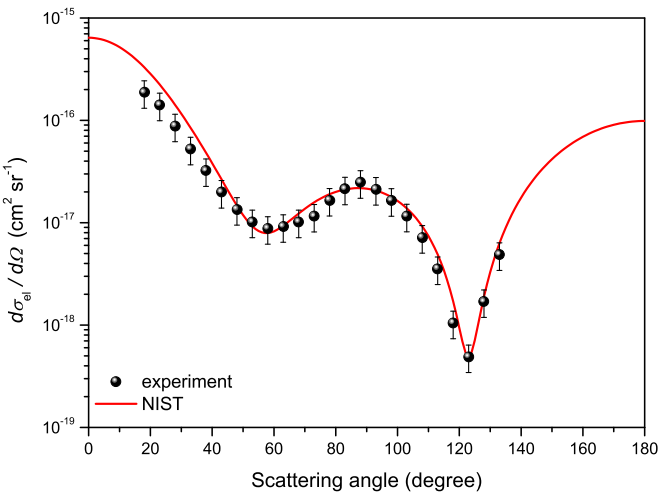

FIG. 3. Experimental (symbols) and theoretical (solid line) differential cross sections of 100 eV electrons scattered elastically by argon. The theoretical values are obtained from the NIST data [40] convolved with a Gaussian with a width equal to the acceptance angle of 2°.

detection angle was adjusted by rotating the spectrometer mounted on the turntable from $\theta = 15^\circ$ to $\theta = 150^\circ$ in 15° steps. They were recorded by repeatedly scanning the electron energy and counting the electrons registered by the channeltrons and dividing the counts by the dwell time for each electron energy point. Typically, three energy scans were performed, and finally, the average was taken.

While the energy spectra of the secondary electrons were measured, the current on the Faraday cup and the pressure reading of the ion gauge were recorded to monitor fluctuations in the beam current and the target density. Exceptions to this procedure were measurements for emission angles below 45° at which the spectrometer housing was blocking the beam path to the Faraday cup. In this case, the beam current was obtained by the interpolation of the values measured before and after the scans at small angles.

For each emission angle, two secondary electron spectra were measured, namely, with and without a gas flow of THF. The latter measurement was done to determine the background in the electron energy spectra. The background signal can be attributed to electrons emitted from residual gas as well as from the metal surface or electronic noise in the detection system. However, the number density of the residual gas was four orders of magnitude lower than that of the gas jet so that the contribution from residual gas could be neglected. For emission angles above 45° the background signal was dominated by the electronic noise. In the measurements at emission angles below 45°, the background spectrum showed increased counts due to secondary electrons produced by protons impacting the surface of the spectrometer housing.

The ranges of secondary electron emission angles and energies for the experimentally determined DDCS in the present work are summarized in Table I. The secondary electron energies were covered in steps of 2.5 eV between 10 and 200 eV, in steps of 10 eV between 200 and 400 eV, and in steps of 20 eV for energies above 400 eV.

D. Uncertainties

The uncertainties in the measurements come from several sources. One source could be attributed to the residual magnetic field inside the chamber, which may affect the path of secondary electrons with low kinetic energies. Assuming a homogeneous magnetic field of 10 μT inside the analyzer, an uncertainty of 6% was estimated for 10 eV electrons. An additional source could arise from the inaccuracy of charge collection of the Faraday cup. This inaccuracy arose due to escaping electrons and was estimated using the measurement results reported by Grusell *et al.* [41]. It amounts to about 4%. Another source might arise due to the nonuniformity of the interaction zone, whose active volume is defined by the overlap of the primary beam and the effusive jet. A variation of the overlap area might affect the count numbers of electrons. Similarly, the misalignment of the gas jet, primary beam, or rotation axis of the spectrometer could cause an angular error.

The statistical uncertainties in count rate measurements were found to be <10% and 10%–50% for electron energies below and above 600 eV, respectively. The larger uncertainties at higher electron energies are due to the poor statistics stemming from a lower ionization cross section and smaller spectrometer transmissions caused by the use of higher CRR values up to 4. The standard deviation for the pressure fluctuation was below 1%, and that for the current was 10%–15%.

The overall relative uncertainties of the DDCS were about 30% for electron energies below 600 eV and 30%–60% otherwise. They were calculated by means of propagation law of all involved uncertainties mentioned above as well as the uncertainties of the literature data [35,42,43] (about 25%) applied in the normalization procedure, which is described in Sec. III.

III. DATA ANALYSIS

Two secondary electron spectra were recorded as a function of electron energy W for each emission angle θ with and without the gas jet in operation. For the data analysis it was assumed that the yield of background events per incident primary particle remained the same in both spectra. According to Eq. (A7) in the Appendix, the ratio of the detected count rates with the gas jet $\dot{N}_{\rm det}^{(g)}(W,\theta)$ to the respective beam current $I_p^{(g)}$ less that of the background count rates $\dot{N}_{\rm det}^{(b)}(W,\theta)$ to $I_p^{(b)}$ is proportional to the double-differential cross section $d^2\sigma_{\rm ion}^{(p)}/dWd\Omega$ for ionization of THF by protons:

$$\frac{\dot{N}_{\rm det}^{(g)}(W,\theta)}{I_p^{(g)}} - \frac{\dot{N}_{\rm det}^{(b)}(W,\theta)}{I_p^{(b)}} = C\frac{p_{g,p}}{T_{g,p}}k_p^{(g)}k_V^{(g)}n_{g,p}(\theta)\eta(W) \times \frac{d^2\sigma_{\rm ion}^{(p)}}{dWd\Omega}(W,\theta)\Delta W\Delta\Omega, \quad (1)$$

where C is a constant defined in Eq. (A8), $p_{g,p}$ is the reading of the ion gauge used for pressure measurement, $T_{g,p}$ is the gas temperature, $k_p^{(g)}$ is the correction factor for gas pressure measurement of THF, $k_V^{(g)}$ is the correction factor for

TABLE I. Proton energies and ranges of secondary electron emission angles and energies covered in the experiments.

	Range of electron energies (eV) versus emission angles									
Proton energy (keV)	15°	30°	45°	60°	75°	90°	105°	120°	135°	150°
300	200	200	200	200	200	200	200	200	200	200
420	800	800	600	600	200	200	200	200	200	200
840	800	800	800	800	200	200	200	200	200	200
1200	800	800	800	800	800	800	200	200	200	200
1550	800	800	800	800	800	600	200	200	200	200
2000	800	800	800	800	800	600	400	400	400	400
3000	400	400	400	800	800	400	400	400	400	400

the pumping speed of the turbomolecular pump, ΔW is the bandwidth of electron energies accepted by the spectrometer, and $\Delta\Omega$ is the solid angle covered by the spectrometer entrance aperture as seen from the center of the interaction zone. The quantity $n_{g,p}(\theta)$ describes the overlap of the primary particle beam and the gas jet. It represents the effective number of target molecules per area divided by the number of target molecules ejected from the nozzle. The quantity $\eta(W)$ is the detection efficiency of the spectrometer for electrons of energy W.

In order to obtain data for correcting the relative energy dependence of the spectrometer's detection efficiency, an electron collision experiment on THF was performed. The electron beam was delivered by the same electron gun used for the characterization of the electron spectrometer. The primary energy of the electron beam was 400 eV. The target number density was chosen to be similar to that in the proton-collision experiments by adjusting the gas supply for the THF gas jet such that the pressure inside the scattering chamber was kept at 10^{-5} mbar. The measurement sequence was the same as in the case of the proton-collision experiments. The relation between the DDCS and the measured quantities is given by

$$\frac{\dot{N}^{(g,e)}_{\rm det}(W,\theta)}{I^{(g)}_{e}} - \frac{\dot{N}^{(b,e)}_{\rm det}(W,\theta)}{I^{(b)}_{e}} = C\frac{p_{g,e}}{T_{g,e}}k^{(g)}_{p}k^{(g)}_{V}n_{g,e}(\theta)\eta(W) \times\frac{d^2\sigma^{(e)}_{\rm ion}}{dWd\Omega}(W,\theta)\Delta W\Delta\Omega, \quad (2)$$

where the meanings of the symbols are analogous to those in Eq. (1). Using the absolute double-differential ionization cross sections $d^2\sigma^{(e)}_{\rm ion}/dWd\Omega$ for electron collision on THF measured by Baek *et al.* [35,42], a correction factor $k_\eta(W,\theta)$ for the relative energy dependence of the detection efficiency $\eta(W)$ is obtained by

$$k_\eta(W,\theta) = \frac{p_{g,e}}{T_{g,e}}\frac{d^2\sigma^{(e)}_{\rm ion}}{dWd\Omega}(W,\theta) \times\left(\frac{\dot{N}^{(g,e)}_{\rm det}(W,\theta)}{I^{(g)}_{e}} - \frac{\dot{N}^{(b,e)}_{\rm det}(W,\theta)}{I^{(b)}_{e}}\right)^{-1}. \quad (3)$$

Using Eq. (2), this correction factor is given by

$$k_\eta(W,\theta) = \frac{1}{Ck^{(g)}_{p}k^{(g)}_{V}\Delta W\Delta\Omega n_{g,e}(\theta)\eta(W)}. \quad (4)$$

Solving Eq. (1) for the DDCS of THF for ionization by protons and using Eq. (4) give

$$\frac{d^2\sigma^{(p)}_{\rm ion}}{dWd\Omega}(W,\theta) = \left(\frac{\dot{N}^{(g)}_{\rm det}(W,\theta)}{I^{(g)}_{p}} - \frac{\dot{N}^{(b)}_{\rm det}(W,\theta)}{I^{(b)}_{p}}\right) \times\frac{T_{g,p}}{p_{g,p}}k_\eta(W,\theta)\frac{n_{g,e}(\theta)}{n_{g,p}(\theta)}. \quad (5)$$

The ratio $n_{g,e}(\theta)/n_{g,p}(\theta)$ is defined as a correction factor $k_n(\theta)$ taking into account that the beam profile and alignment in the electron measurements may be different from the case of the measurements with protons:

$$k_n(\theta) = \frac{n_{g,e}(\theta)}{n_{g,p}(\theta)}. \quad (6)$$

This correction factor was derived using the measured secondary electron spectra after proton impact on argon for a subset of proton beam energies and emission angles covered in the literature data published by Rudd *et al.* [43]. The measurement was done in the same way as described above for THF. In these experiments, the measurement equation is given by

$$\frac{\dot{N}^{(g)}_{{\rm det},Ar}(W,\theta)}{I^{(g)}_{p,Ar}} - \frac{\dot{N}^{(b)}_{{\rm det},Ar}(W,\theta)}{I^{(b)}_{p,Ar}} = C\frac{p_{g,Ar}}{T_{g,Ar}}k^{(Ar)}_{p}k^{(Ar)}_{V}n_{Ar,p}(\theta)\eta(W) \times\frac{d^2\sigma^{(p)}_{{\rm ion},Ar}}{dWd\Omega}(W,\theta)\Delta W\Delta\Omega, \quad (7)$$

where the meanings of the symbols are analogous to those in Eq. (1). For those emission angles and proton and secondary electron energies for which literature data were available [43], a calibration factor could be defined by

$$f_{\rm cal}(\theta) = [k_\eta(W,\theta)]^{-1}\frac{p_{g,Ar}}{T_{g,Ar}}\frac{d^2\sigma^{(p)}_{{\rm ion},Ar}}{dWd\Omega}(W,\theta) \times\left(\frac{\dot{N}^{(g)}_{{\rm det},Ar}(W,\theta)}{I^{(g)}_{p,Ar}} - \frac{\dot{N}^{(b)}_{{\rm det},Ar}(W,\theta)}{I^{(b)}_{p,Ar}}\right)^{-1}. \quad (8)$$

Using Eqs. (6) and (7), this calibration factor is equivalent to

$$f_{\rm cal}(\theta) = \frac{k^{(g)}_{p}}{k^{(Ar)}_{p}}\frac{k^{(g)}_{V}}{k^{(Ar)}_{V}}\frac{n_{g,p}(\theta)}{n_{Ar,p}(\theta)}k_n(\theta). \quad (9)$$

Variations of the overlap integral between the proton beam and gas jet as described by $n_{g,p}(\theta)$ and $n_{Ar,p}(\theta)$ are expected to be negligible in comparison to other sources of uncertainty. Therefore, the correction factor $k_n(\theta)$ can be obtained as

$$k_n(\theta) = f_{\rm cal}(\theta)\frac{k^{(Ar)}_{p}}{k^{(g)}_{p}}\frac{k^{(Ar)}_{V}}{k^{(g)}_{V}}. \quad (10)$$

To determine the correction factors for the different pumping speeds, flow characteristics, and ion gauge (calibrated for nitrogen) sensitivities of argon and THF, an additional pressure measurement in the gas reservoir was performed by using a capacitance manometer (Baratron) whose reading is known to be independent of gas type. The readings of the ion gauge were plotted against those of the Baratron, and the ratio $k^{(Ar)}_{p}k^{(Ar)}_{V}/k^{(g)}_{p}k^{(g)}_{V}$ was determined by linear regression of the data. It amounted to 0.243 ± 0.001.

The SDCS were derived from the DDCS determined according to Eq. (5). Two different procedures were applied depending on the energy range of the secondary electrons. Due to the limited energy range of secondary electrons covered in the measurements, the experimental SDCS were obtained between 10 and 200 and 10 and 400 eV for protons with energies below 1550 keV and above 2000 keV, respectively. For electron energies below 200 eV, a superposition of Lorentzian functions was applied to model the measured DDCS as a function of the emission angle. The motivation for using this model was given by Rudd [44]. In our model function, one Lorentzian term was used to reproduce the binary peak occurring at emission angles between 45° and 75°, while the other two terms were used to fit the extrapolated DDCS in the forward (below 15°) and backward directions (above 150°),

respectively. The integration of DDCS model functions over the emission angles yields the SDCS for electron energies below 200 eV. However, this procedure is unable to fit the measured DDCS in the energy range between 200 and 400 eV due to the contribution from Auger electrons. For the sake of the data completeness, the SDCS in this energy range were obtained from the experimental DDCS using the trapezoidal rule and assuming the DDCS is flat in the forward (below 15°) and backward directions (above 150°). The TICS were calculated by integrating the SDCS using the trapezoidal rule over the range of secondary electron energies with an energy resolution in 1 eV steps. In this calculation, the SDCS below 10 eV were assumed to have the same value as that at 10 eV.

IV. THEORY

Due to the lack of other experimental data for the DDCS for proton impact on THF, our results were compared to theoretical models, namely, the Hansen-Kocbach-Stolterfoht (HKS) equation [45], and a new methodology based on the dielectric response function formalism (DRF) [25].

The HKS model is a semiempirical model for the DDCS based on the impact parameter's first Born approximation [45,46]. The descriptions of the initial and final electron states are approximated by hydrogenic and plane-wave functions, respectively. Some parameters in the HKS model were derived empirically to improve its consistency [45]. The advantage of the HKS model is that it provides an analytical expression, requiring only the binding energies of electrons in the respective atom or molecule.

The semiempirical model based on DRF has been recently proposed for calculating the double-differential ionization cross sections of condensed organic materials impacted by swift ions [25]. It represents an extension of a previous work, which was limited to SDCS and TICS [24]. The model is based on the dielectric formalism [47,48] and exploits the dependence of the electronic excitation spectrum of the target on the transferred energy $\hbar\omega$ and momentum $\hbar k$ in order to obtain the cross section as a function of the secondary electron kinetic energy W and of the ejection angle θ.

The cross section for ejecting electrons of energy W in a solid angle $d\Omega = 2\pi \sin(\theta) d\theta$ from a molecular orbital j by an ion of mass M and atomic number Z moving with energy T in a medium of dielectric function $\epsilon(\hbar k, \hbar\omega)$ is given, within this method, by

$$\left.\frac{d^2\sigma(W,\theta)}{dW d\Omega}\right|_j = \frac{\alpha e^2}{2\pi^2 \hbar^2 N \sin\theta} \frac{M[Z-\rho(k)]^2}{T} \mathrm{Im}\left[\frac{-1}{\epsilon(\hbar k, B_j + W)}\right]_j \times \frac{\sqrt{T[T-(B_j+W)]}\sin(\alpha\theta)}{2T-(B_j+W)-2\sqrt{T[T-(B_j+W)]}\cos(\alpha\theta)} \times F_{\mathrm{Salin}}(T,M,W,B_j,\theta), \quad (11)$$

where the expression $\hbar\omega = B_j + W$ is used.

Here, $\rho(k)$ is the Fourier transform of the electronic density of the projectile, which is calculated according to the Brandt-Kitagawa model [49]. The quantity B_j is the binding energy of the molecular orbital j, or the mean binding energy of the outer shell electrons, as explained elsewhere [24,25]. The target is characterized by its number density N for the condensed target and the energy-loss function (ELF) $\mathrm{Im}[-1/\epsilon(\hbar k, \hbar\omega)]_j$, which represents its electronic excitation spectrum. The subscript j in the ELF refers to the contribution coming from the specific shell j. The parameter α is derived from the binary encounter approximation, $\alpha = \phi_{\max}/\theta_{BE}$, where $\theta_{BE} = \arccos(\sqrt{MW/4mT})$ is the binary peak electron ejection angle and $\phi_{\max}$ is the scattering angle of the projectile at which the ionization cross section is maximum [25]. The quantity m is the electron mass. Salin's factor $F_{\mathrm{Salin}}(T,M,W,B_j,\theta)$ semiempirically accounts for the enhanced forward electron ejection due to the electron capture to the continuum process [2,50,51].

Basically, this method calculates the inelastic scattering DDCS $d^2\sigma/d\omega dk$ within the dielectric formalism [52]. The electron kinetic energy and ejection angle are related to the excitation energy and momentum by $\hbar\omega = B_j + W$, and $\hbar k = \sqrt{2M[2T - \hbar\omega - 2\sqrt{T(T-\hbar\omega)}\cos(\phi)]}$. Such relations allow obtaining the DDCS as a function of the projectile scattering angle ϕ if the ELF is known over the whole energy and momentum plane (the Bethe surface). The electron ejection angle θ is related to ϕ via $\theta = \phi/\alpha$ [25].

The advantage of this method is that the knowledge of the ELF and the mean binding energy of the outer-shell electrons of the target material is enough to obtain the DDCS. The ELF is usually obtained from experimental data in the optical limit ($k = 0$) and is extended to arbitrary values of the momentum transfer through different dispersion relations [53]. The Mermin energy-loss-function–generalized-oscillator-strength (MELF-GOS) method [54] represents an adequate dispersion algorithm, yielding good angular dependencies [25]. Nonetheless, even if the ELF for the material of interest is not experimentally known, it can be approximately predicted through an empirical parametrization for organic materials that only needs as input the atomic composition and density [55]. Therefore, the method is applicable to virtually any organic material.

In this work, since there is no experimental information available for the optical ELF of THF, it has been obtained using a semiempirical parametric model. The binding energies of the electronic levels have been calculated by means of GAMESS [56], applying the restricted Hartree-Fock (RHF) method and the 6-311G basis set. As orbital energies calculated by the RHF method may be different from the vertical ionization energy [57], the binding energies of the outermost valence electrons were substituted by experimental values, yielding a mean binding energy for the outer shell electrons of 18.93 eV. The inner shells considered are the K shells of carbon and oxygen with binding energies of 284.2 and 543.1 eV, respectively. It has to be noted that, apart from using an approximate ELF, another source of uncertainty is that this method is developed for condensed phase materials, while the experiments are performed in the gas phase.

V. RESULTS AND DISCUSSION

Figure 4 shows a comparison of experimental cross sections of different biomolecules for 2000 keV protons as a function of secondary electron energy in a sequence of emission angles

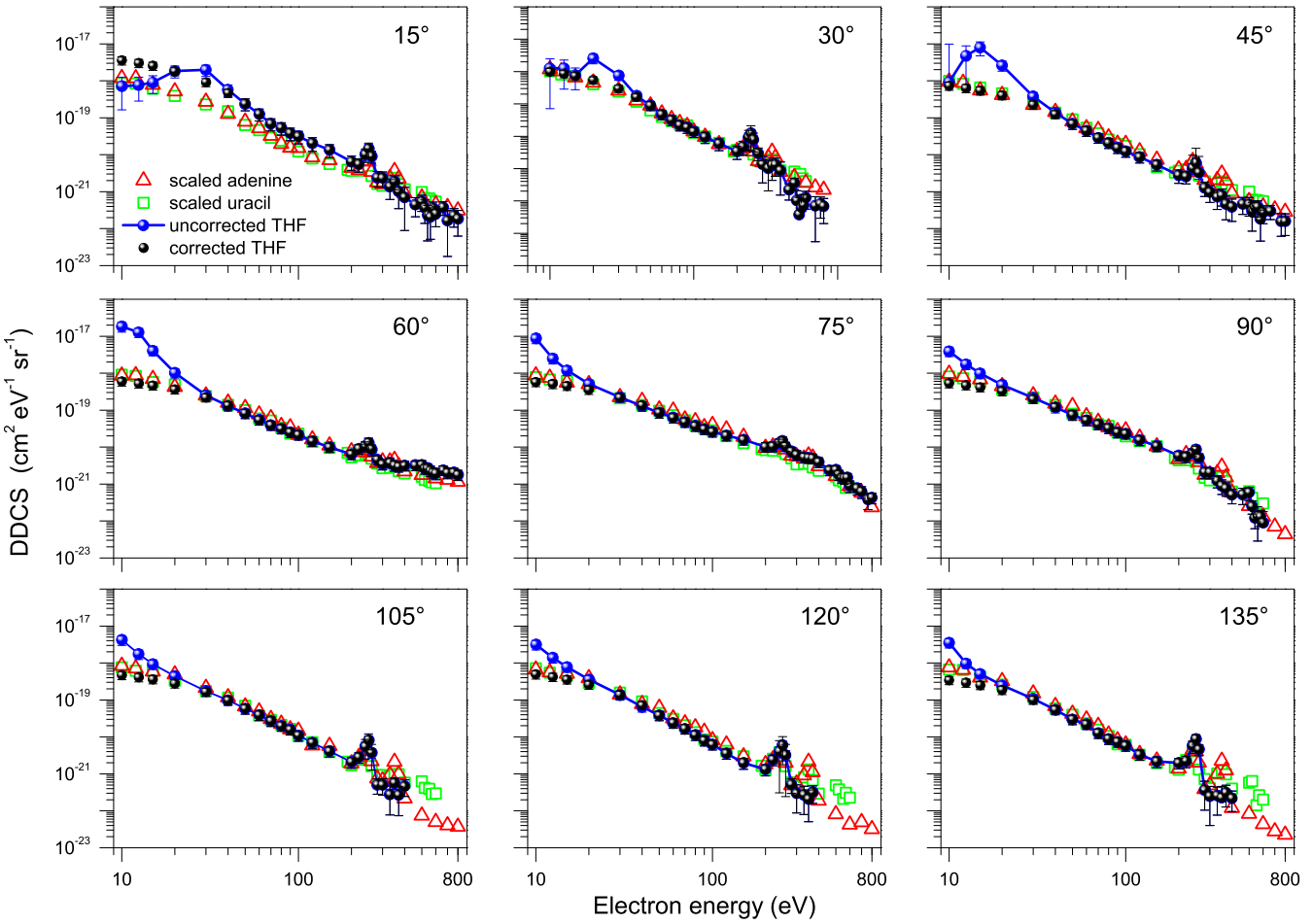

FIG. 4. Uncorrected (blue dots) and corrected (black dots) experimental double-differential cross sections (DDCS) for ionization of THF by 2000 keV protons in comparison to the DDCS of adenine (red open triangles) and uracil (green open squares) reported by Itoh *et al.* [21,22]. The reason and method used for the correction are explained in the text. The data are shown as a function of secondary electron energy for a sequence of emission angles from 15° to 135°. The data sets of adenine and uracil were scaled with a factor 30/50 and 30/42, representing the ratio of the number of valence electrons.

from 15° to 135° in 15° steps. Our measured DDCS of THF are compared to the DDCS of adenine and uracil reported by Iriki *et al.* and Itoh *et al.* [21,22]. Adenine and uracil are both larger than THF and known as complex molecules of nucleobases. To enable a comparison independent of the molecular size, the data from Iriki *et al.* and Itoh *et al.* were multiplied by the ratio of the number of valence electrons in THF to those in adenine or uracil. At energies below 50 eV, the procedure described in Sec. III has not been efficient at removing the signal contribution of detected electrons created by protons hitting the metal surface, especially at small incident angles. To solve this problem, the measured DDCS for the energies below 50 eV were extrapolated from the values at higher energies by using the same relative energy dependence as for argon data from the literature [43]. The corrected DDCS of THF are in quite good agreement with the scaled data for adenine and uracil. However, it has not been possible to apply this correction procedure to the data at the 150° emission angle because the argon literature data [43] did not cover such large emission angles.

Our experimental data are compared to the theoretical DDCS calculated by the HKS model [45] and the DRF [25] model for protons with incident energies from 300 to 3000 keV. Figures 5 and 6 show the complete set of measured data as a function of electron energy for the different emission angles, while in Fig. 7 the angular dependence is depicted for selected electron energies. Both theoretical models reproduce the general trends of the experimental data. The agreement between experimental and theoretical data becomes better with increasing proton energies as they approach the optical limit [2]. Thus, the best agreement for low electron energies was found at a proton energy of 2000 keV. The Auger electrons ejected from carbon and oxygen atoms appear in the experimental data at energies between 200 and 300 eV and between 400 and 500 eV, respectively, whereas the Auger processes are not included in the theoretical calculations.

At 15° emission angle, both models predict lower absolute values, especially at electron energies below 100 eV (see Fig. 5). The experimental data are larger than the DRF data and HKS data by a factor of up to 5 and 15, respectively. The DRF data also show better agreement with the experimental results at a small angle of 30°. This better agreement may come from the consideration of a more realistic electronic excitation spectrum of THF, which is accounted for in the

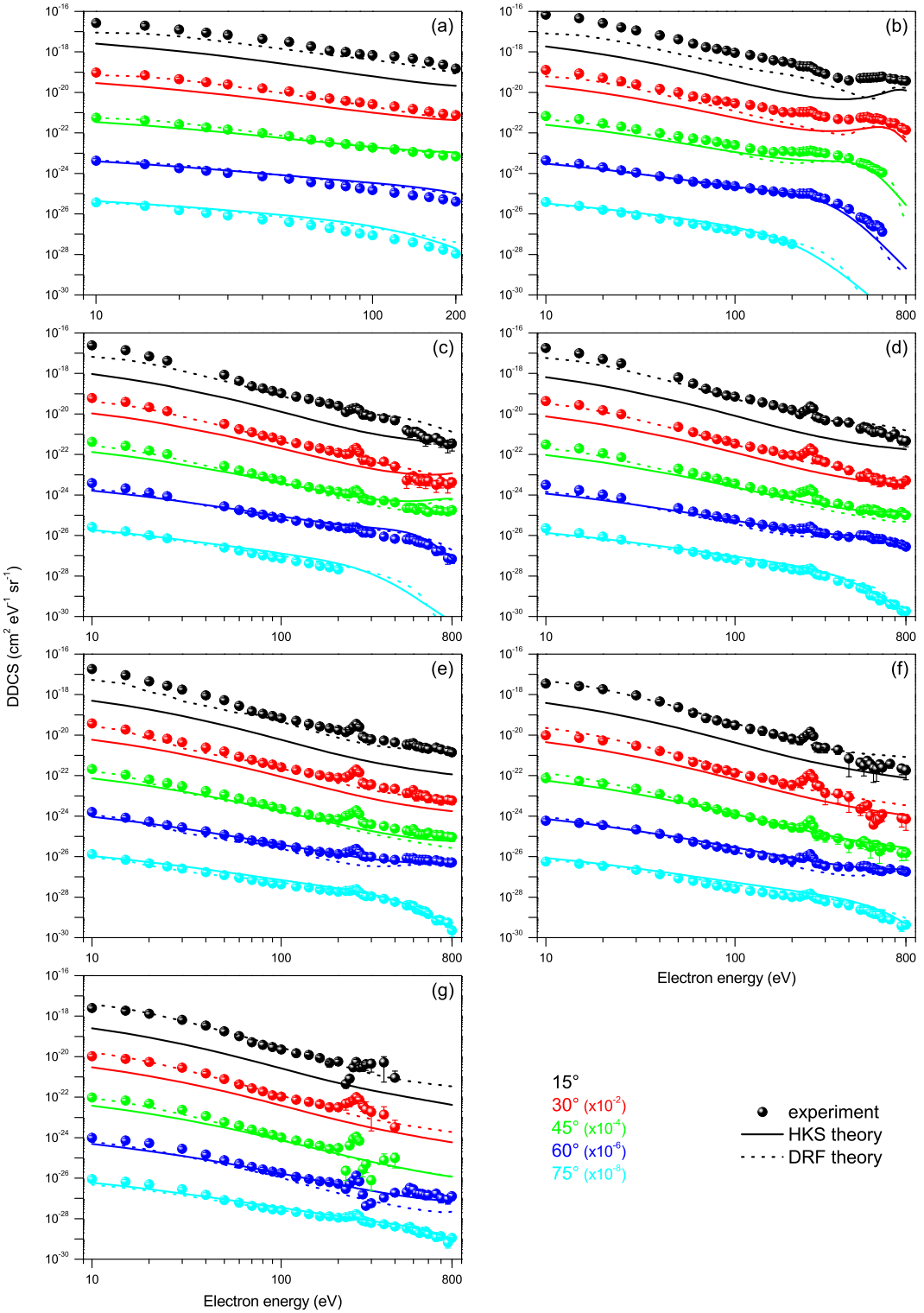

FIG. 5. Present experimental (symbols) double-differential cross sections (DDCS) for ionization of THF by protons in comparison to the theoretical DDCS obtained using the HKS model [45] (solid line) and the DRF model [25] (dashed line) for different proton energies: (a) 300, (b) 420, (c) 840, (d) 1200, (e) 1550, (f) 2000, and (g) 3000 keV. The results are shown as a function of secondary electron energy for the emission angles from 15° to 75°. For readability, the data of different emission angles are multiplied by the indicated factor.

DRF calculation by the use of the energy-loss function. In the HKS model, the target electron is just described by a hydrogenic wave function and hence describes its electronic excitation spectrum in a less accurate way. Moreover, both models are based on the first Born approximation. Since the first Born approximation does not take into account two-center effects [25], it is unable to reproduce the process of electron capture to the continuum (ECC). In this process, electrons

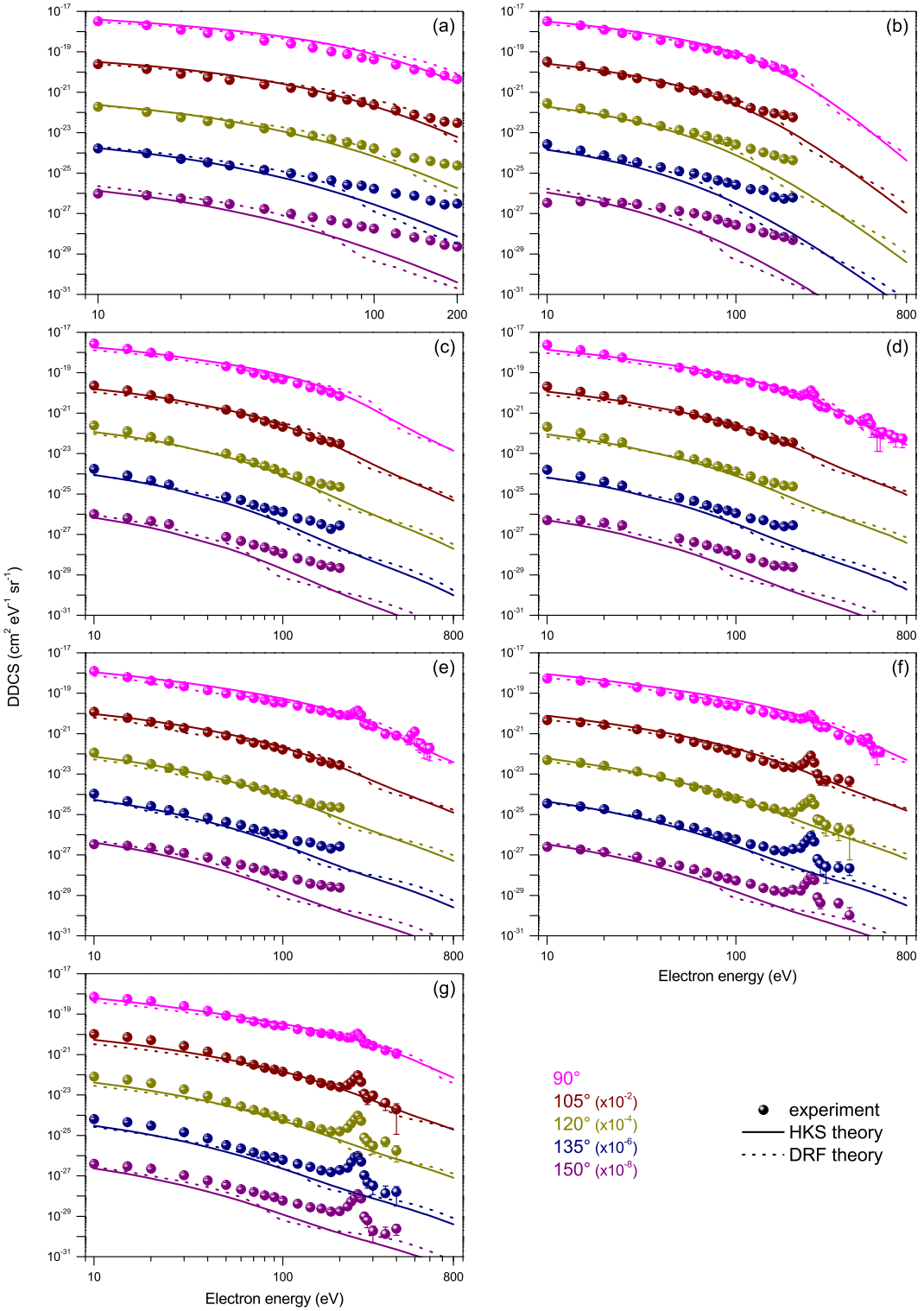

FIG. 6. The same as in Fig. 5, but for the emission angles from 90° to 150°.

ejected from the target with velocities similar to those of the projectile ions are attracted by the leaving ions. Hence, they are essentially focused in the forward direction. In the DRF calculation using Eq. (11), the two-center effect was considered by the introduction of Salin's factor [50]. It is a multiplicative factor whose essential part is proportional to $|\vec{v}_p - \vec{v}_e|^{-1}$, where $\vec{v}_p$ and $\vec{v}_e$ are the velocities of the projectile ion and of the secondary electron, respectively. Thus, this factor enhances the DDCS when $\vec{v}_e$ approaches $\vec{v}_p$. As an example, Fig. 8 shows that for the 1200 keV proton impact the introduction of Salin's factor improves the prediction in the forward direction, especially for electron energies corresponding to velocities similar to that of the incoming proton (e.g., $W = 500$ eV) and also for electrons of lower

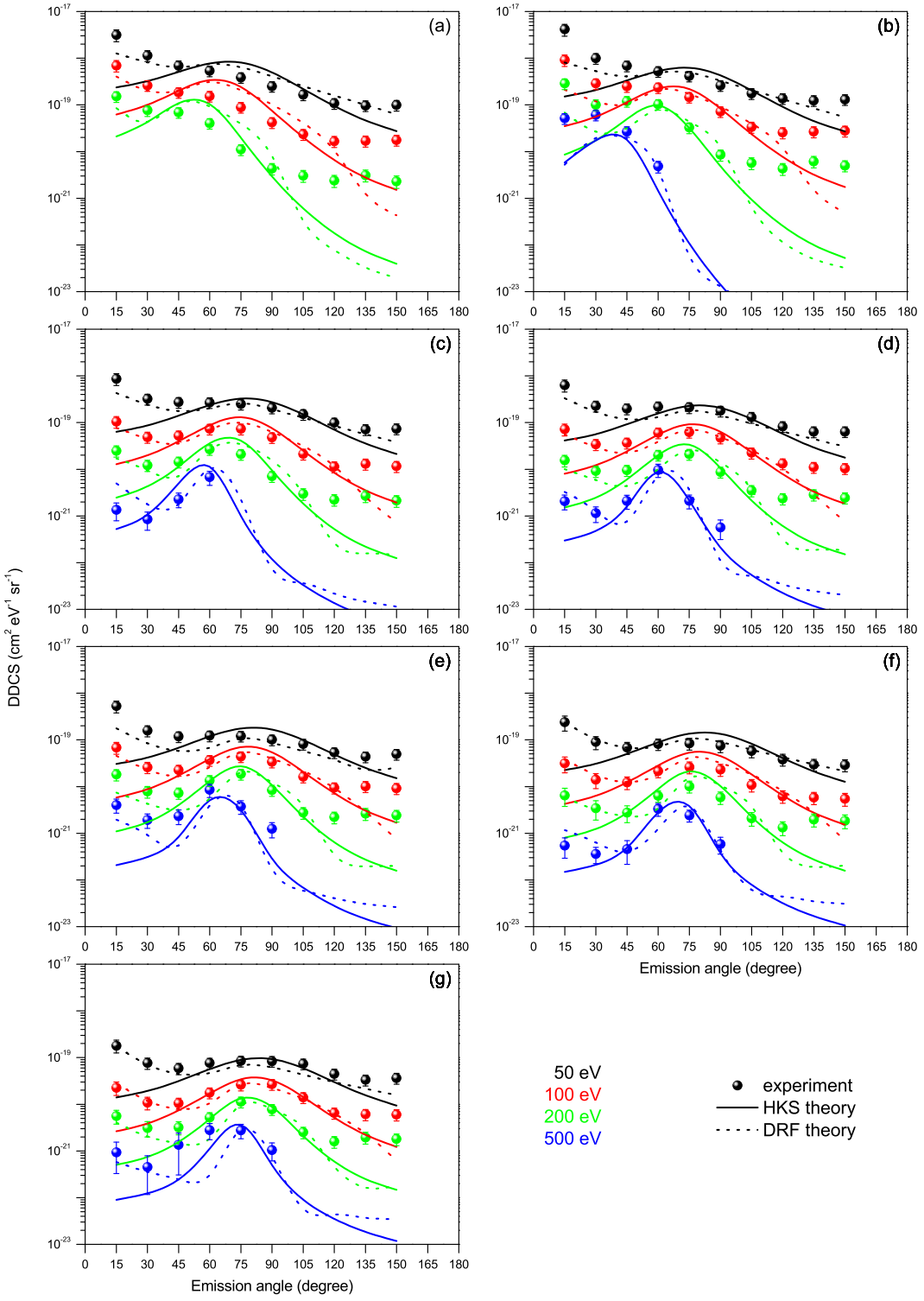

FIG. 7. Present experimental (symbols) double-differential cross sections (DDCS) for ionization of THF by protons in comparison to the theoretical DDCS obtained using the HKS model [45] (solid line) and the DRF model [25] (dashed line) for different proton energies: (a) 300, (b) 420, (c) 840, (d) 1200, (e) 1550, (f) 2000, and (g) 3000 keV. The results are shown as a function of emission angle for secondary electron energies 50 eV (black), 100 eV (red), 200 eV (green), and 500 eV (blue).

energies (e.g., $W = 50$ eV), which experience the potentials of both the target and outgoing proton at the same time.

At emission angles θ between 45° and 105° the agreement between the HKS and DRF models improves. As can be seen from Figs. 5 and 6, both models can reproduce the energy dependency of the present experimental data at secondary electron energies up to 200 eV for primary proton energies below 840 keV and at energies up to 800 eV for primary proton energies above 1200 keV. In this region of emission angles θ between 45° and 105°, the binary encounter peak

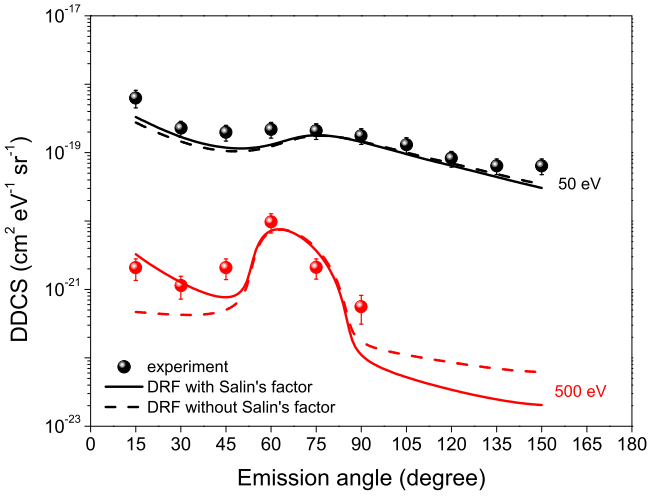

FIG. 8. Present experimental (symbols) double-differential cross sections (DDCS) for ionization of THF by 1200 keV protons in comparison to the theoretical DDCS obtained using the DRF model [25] with (solid line) and without (dashed line) Salin's factor [50]. The results are shown as a function of emission angle for secondary electron energies 50 eV (black) and 500 eV (red).

is a dominant feature in angular distributions (see Fig. 7). This is a direct consequence of hard collisions, for which there is a large energy transfer from the projectiles to target electrons [2]. The DRF model predicts a fairly good description of the experimental data in this angular range for protons with energies above 420 keV, except for some data points at 45°, which are underestimated, particularly for electron energies above 200 eV. At a proton energy of 300 keV, the results of the DRF model are higher than the experimental data by a factor of up to 5 at the peak maximum. On the other hand, the HKS model is able to reproduce the peak position but generally overestimates the maximum by a factor of up to 5.

At emission angles θ between 120° and 150° (see Fig. 6), the agreement between both calculations and measurements is acceptable at low electron energies ($W < 50$ eV) but worsens remarkably with increasing ejected electron energies (by a factor of up to 200 at $W = 200$ eV and $\theta = 150°$). Both models fail to predict cross sections of collisions involving larger emission angles in combination with high-energy transfer ($W > 100$ eV). One of the reasons for this discrepancy may be the simplified description at high momentum transfer as the electron emission in backward directions involved a scattering on the full nucleus charge [4,45]. Since in the DRF model the binary encounter peak position is used to determine the position of the maximum in the DDCS, the calculations are more uncertain in the angular region far away from the binary peak [25], while the hydrogenic wave function used in the HKS model leads to a screening of the nucleus charge. Another reason may be that the use of a plane-wave function is not accurate enough to describe the emitted electrons [4] in this case.

Scalability of differential cross sections has been investigated by Toburen and Wilson for water molecules [12] and for numerous hydrocarbon molecules [58] and was recently verified by Iriki *et al.* for adenine [20] as complex molecular targets by 1 MeV proton impacts. According to the above research, the scaling with the number of valence electrons n_v in molecules is found to be a good approximation of these ionization cross sections. This approximation is valid for large impact parameters where a fast charged projectile predominantly interacts with the weakly bound valence electrons. Figure 9 shows the angular distribution of experimental data for THF (C_4H_8O, $n_v = 30$) at electron energies 15, 50, 200, and 500 eV by protons of 300, 1550, and 2000 keV. The present results of THF are compared to the data for hydrogen (H_2, $n_v = 2$) [59], water vapor (H_2O, $n_v = 8$) [12], ethane (C_2H_6, $n_v = 14$) [58], benzene (C_6H_6, $n_v = 30$) [58], uracil ($C_4H_4N_2O_2$, $n_v = 42$) [22], and adenine ($C_5H_5N_5$, $n_v = 50$) [21]. The DDCS of the respective molecule were multiplied by the ratio of the number of the valence electrons of THF to that of their valence electrons.

Generally, the data for molecular hydrogen differ from those for other polyatomic molecules at small and large emission angles. The emitted secondary electrons from the hydrogen are more anisotropic than those from other molecules. This is due to the momentum distribution of the target electrons, which are broader in polyatomic molecules compared to hydrogen [58].

Note that benzene has the same number of valence electrons and a ring structure similar to that of THF, while that is not the case for ethane, which, nonetheless, shows a similar scaled DDCS. As Wilson and Toburen [58] pointed out, neither angular nor energy distributions within the hydrocarbon groups are influenced very much by the variations in molecular bondings, namely, the C-H bond; single, double, and triple C-C bonds; and the chemical structure. Compared to THF, most of those polyatomic molecules have different numbers of valence electrons and individual chemical structures, but the angular distribution of scaled data for these molecules shows reasonable agreement for a wide range of emission angles except for $\theta = 15°$, where the DDCS of THF are significantly higher than that of other molecules. This is particularly pronounced at low electron energies. As can be seen from Fig. 9, this increase in the angular distribution for THF at forward angles is also predicted in the DRF calculation rather than in the HKS calculation since the former model considers the realistic electronic excitation of the spectrum of THF by means of the energy-loss function. However, it is interesting that such a larger increment with a factor of up to 10 compared to DRF data was observed from experimental results at $\theta = 15°$. Further investigation of this property is indeed required.

At a proton energy of 300 keV, the results of THF exhibit a less peaked angular distribution than hydrocarbons, one that is more similar to that of water vapor. An explanation is that the target electrons in the outer orbits in THF or water molecules have higher average kinetic energies than those of hydrocarbons; therefore, they also have a broader momentum distribution [3]. The difference in angular distributions of water and hydrocarbons was intensively studied by Wilson and Toburen [58]. Unfortunately, Iriki *et al.* [20] did not include their data at 0.5 MeV in the comparison, which would have already shed light on an expected difference in the angular distribution due to the lower proton energy and hence a greater contribution of two-center effects.

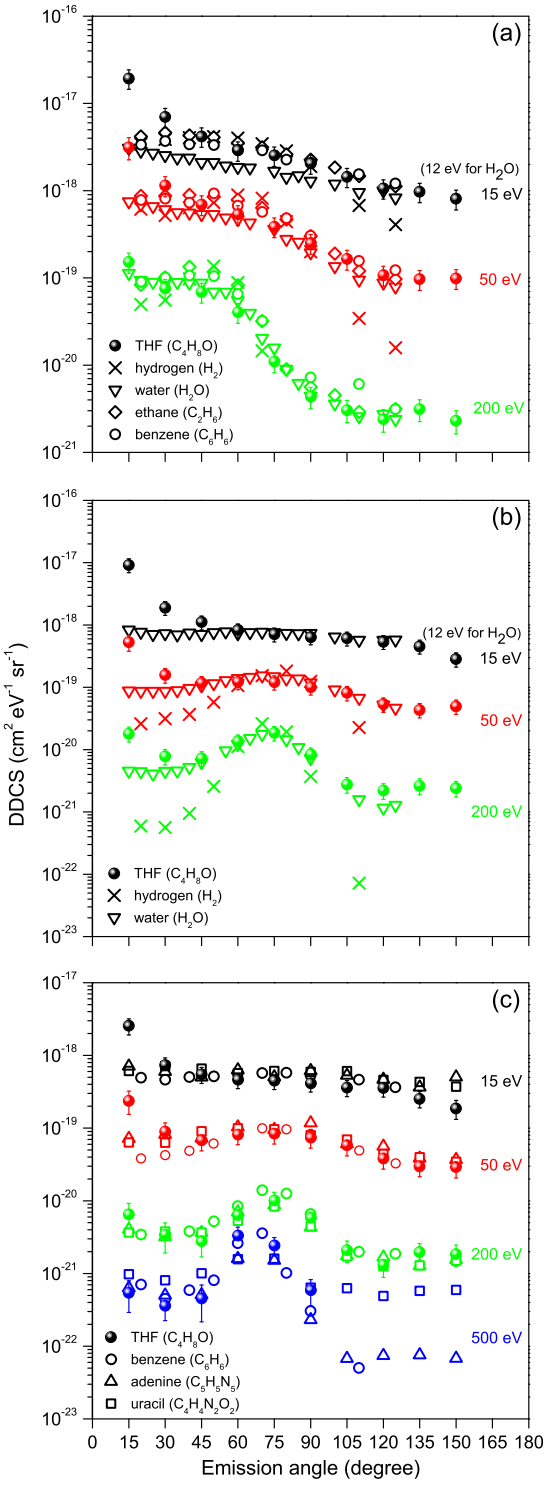

FIG. 9. Present experimental (symbols) double-differential cross sections (DDCS) for ionization of THF by protons with incident energies of (a) 300, (b) 1550, and (c) 2000 keV. The results are compared to the DDCS of hydrogen [59], water [12], ethane and benzene as hydrocarbon [58], adenine [21], and uracil [22] for different proton energies: (a) 0.3, (b) 1.5, and (c) 2.0 MeV. The data are shown as a function of emission angle for secondary electron energies 15 eV (black), 50 eV (red), 200 eV (green), and 500 eV (blue). The data sets of other molecules were multiplied by the ratio of the number of the valence electrons of THF to that of their valence electrons.

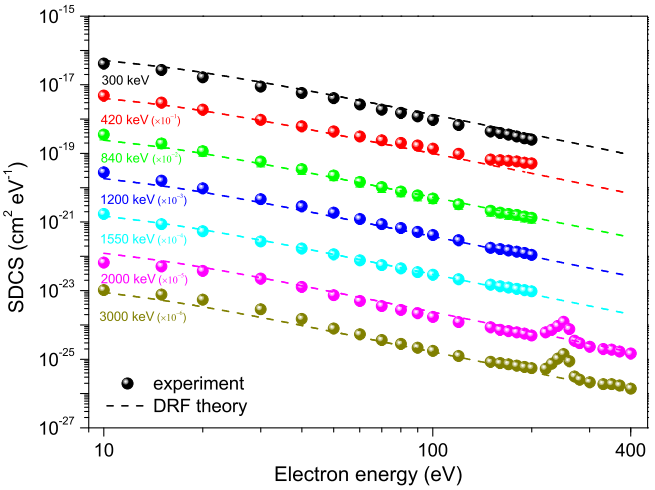

FIG. 10. Present experimental (symbols) single-differential cross sections (SDCS) for ionization of THF by protons as a function of secondary electron energy. The data were obtained from the DDCS by numerical integration over the solid angle. The present results are compared to the theoretical SDCS calculated using the DRF model [24] (dashed line) for different proton energies. For better readability, the data for the different proton energies are multiplied by the indicated factor.

When the incident proton energy increases, the angular distribution of lower electron energies appears more isotropic since those electrons below a few tens of electronvolts are produced predominantly by distant collisions. For higher electron energies, the binary encounter peak becomes relatively more apparent and sharper. This is due to the decreasing influence of the binding energy of the target electron: the binding energy becomes negligible compared to the energy transferred in a hard collision. At a proton energy of 2000 keV, the present data for THF are compared to those for other complex targets, and they are found to be nearly identical at electron energies of 15, 50, and 200 eV. The disagreement between uracil and the other molecules at higher electron energy $W = 500$ eV, especially for large angles $\theta \geqslant 105^\circ$, arises from the Auger electron emissions of the oxygen atom in the uracil molecule.

Figure 10 shows a comparison of the present results with the theoretical calculations of SDCS based on the DRF model [24]. Experimental results are in quite good agreement with DRF calculations over a wide range of incident proton and secondary electron energies. As SDCS were governed by electrons from the binary encounter peak, differences in backward scattering observed in DDCS play a minor role. Peak structures attributed to Auger electrons from carbon were observed in the experimental spectra at about $W = 250$ eV for proton energies of 2000 and 3000 keV. A discrepancy was observed in the region around $W = 200$ eV at 420 keV proton energy. A possible explanation is the contribution from the electrons involved in the ECC process, as for 420 keV protons the left wing of the ECC peak (around 230 eV) is within the measured energy range. However, with this explanation the effect of ECC should also be observed around 160 eV for the case of 300 keV protons. Therefore, the reason for this discrepancy remains an open question.

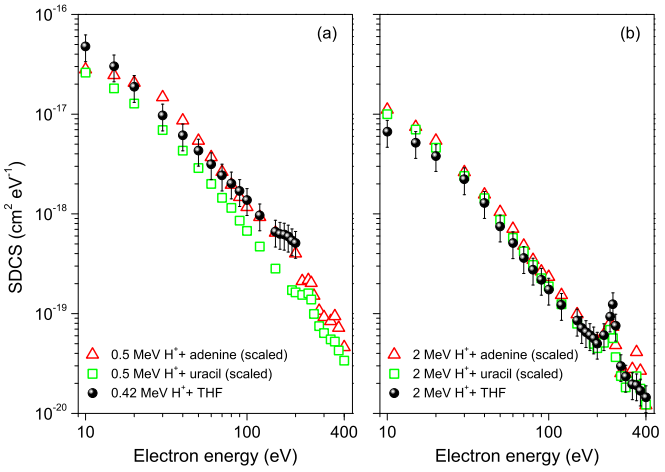

FIG. 11. Present experimental (black dots) single-differential cross sections (SDCS) for ionization of THF by protons with incident energies of (a) 420 and (b) 2000 keV. The data were obtained from the DDCS by numerical integration over the solid angle. The results are compared to the SDCS of adenine (red open triangles) and uracil (green open squares) reported by Itoh *et al.* [20–22] for different proton energies: (a) 0.5 and (b) 2 MeV. The data sets of adenine and uracil were multiplied by the ratio of the number of the valence electrons of THF to that of their valence electrons.

As shown in Fig. 11, in order to check the scalability of SDCS, the data for THF are compared to those for adenine [20,21] and uracil [22] multiplied by the ratio of the number of valence electrons of THF to that of their valence electrons. The nitrogen Auger peak occurs in Itoh's data at about $W = 350$ eV since both adenine and uracil contain nitrogen. The SDCS for ionization of THF by 2000 keV proton impact are in quite good agreement with those of uracil except at $W = 10$ eV, where the latter are higher by a factor of 2. When the data for ionization of THF by 420 keV protons are compared to Itoh's data at 0.5 MeV proton energy, good agreement between the data for THF and the scaled data for adenine is observed for electron energies above 50 eV, while at lower electron energies ($W < 50$ eV) they disagree by a factor of up to 2. However, the scaled SDCS of uracil are consistently lower than these of adenine at 0.5 MeV protons, indicating that it may be questionable to apply the scaling procedure at low proton energies.

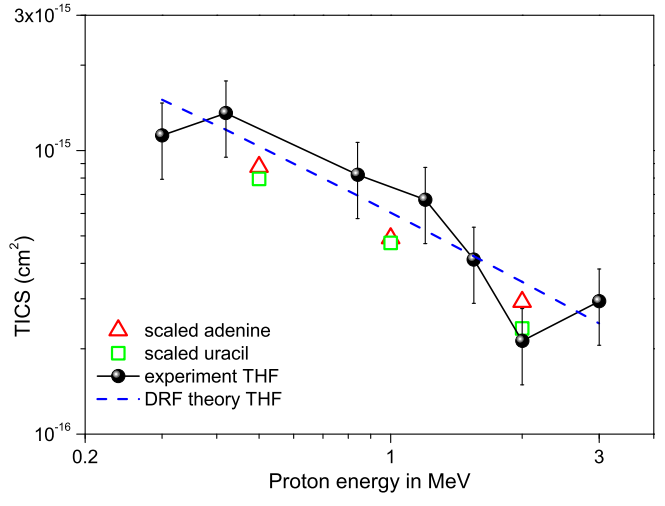

FIG. 12. Present experimental (black dots) total ionization cross sections (TICS) of THF obtained by integrating the SDCS in comparison to the theoretical TICS of THF calculated using the DRF model [24] (blue dashed line) for different proton energies. The TICS of adenine (red open triangles) and uracil (green open squares) reported by Itoh *et al.* [20–22] are also shown for proton energies at 0.5, 1, and 2 MeV. The data sets of adenine and uracil were scaled by the ratio of the number of valence electrons.

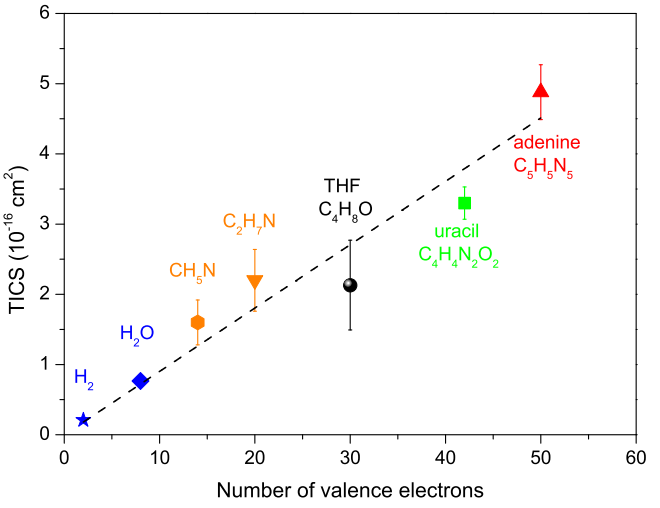

FIG. 13. The experimental total ionization cross sections (TICS) of various molecules for 2 MeV proton impact as a function of the number of valence electrons. The data are taken from [1] for molecular hydrogen (H_2), from [13] for water (H_2O), from [60] for monomethylamine (CH_5N) and dimenthylamine (C_2H_7N), from [22] for uracil ($C_4H_4N_2O2$), and from [21] for adenine ($C_5H_5N_5$). The TICS of THF is also plotted.

Figure 12 shows the TICS of THF as a function of incident proton energy together with theoretical results calculated using the DRF model [24] as well as the TICS of adenine [20,21] and uracil [22], scaled by the number of valence electrons. The theoretical values are mostly within the uncertainties of present TICS, which are estimated to be of the order of 30%.

Finally, the scaling property of TICS is discussed as follows. As a simple additivity rule to determine the TICS, it was previously studied for polyatomic [1] and amine [60] molecules and recently verified for adenine [20,21] ($n_v = 50$) and uracil [22] ($n_v = 42$). Figure 13 illustrates the TICS of those molecules as a function of the number of valence electrons at 2 MeV proton impact, together with the present result for THF ($n_v = 30$). The dashed line in Fig. 13 represents the results of linear regression (with intercept zero). The fit was obtained by weighting the data points with the inverse square of uncertainties. The slope of the scaling line is obtained as $(0.090 \pm 0.005) \times 10^{-16}$ cm^2, compared to 0.094×10^{-16} cm^2 given by Itoh *et al.* [22].

VI. CONCLUSION

We reported the measurements of the DDCS for proton-impact ionization of THF, which is a structural analog to the sugar part of DNA. The proton energy range was between 300

and 3000 keV. The measurements were carried out using a crossed-beam configuration and an electrostatic hemispherical electron spectrometer to detect the secondary electrons. The secondary electron spectra were measured at observation angles between 15° and 150° in 15° steps relative to the direction of the incident proton beam. These spectra were converted indirectly into absolute cross sections using DDCS of THF for 400 eV electrons [35,42] and the published cross-section data for argon for protons [43].

The experimental DDCS were compared with the HKS model [45] and a recently reported DRF model [25]. Both of them could reproduce the general trends of the experimental data. In particular, the DRF data show better agreement with the experimental results in the region of the binary peak and for small emission angles. This improved prediction of the DRF model, which is based on the realistic electronic excitation spectrum of the target, indicates that the use of atomic models for a complex target such as THF is not sufficient for fully reproducing the experimental DDCS. At large emission angles, the underestimation of experimental DDCS by both models is due to the simplified description of the scattering process close to the nucleus.

The scalability of experimental DDCS for THF was checked by comparing the angular distributions of molecular hydrogen [59], chosen as a simple target, and a variety of polyatomic molecules [12,20–22,58]. While the DDCS of molecular hydrogen is similar only near the binary peak, the data for the other polyatomic molecules, including THF, for protons with energies above 420 keV are found to scale fairly well for a wide range of emission angles, despite the individual chemical structures in the respective molecules. However, this comparison also implies that the peak shape could be dependent on the momentum distribution of the target electrons in the molecule, particularly at low proton energies. It is noteworthy that an increase in experimental DDCS for THF was observed at small emission angles, as predicted in the DRF calculation. Further investigation is necessary to understand the discrepancy between experiment and theory at 15°.

SDCS and TICS of THF obtained by integration of DDCS show good agreement with the theoretical values calculated using the DRF model [24]. In comparison to the data for adenine [20,21] and uracil [22] scaled by the number of valence electrons, it seems that the scaling property of SDCS is only valid for large impact parameters, i.e., for protons of 2 MeV, and fails for lower proton energies around 0.5 MeV. The TICS of various molecules [1,13,21,22,60], including THF, at 2 MeV confirm the scaling law [1], which means the TICS linearly increases with the number of weakly bound electrons of molecules. This is due to the fact that the ionization cross sections gets its largest contribution from collisions between protons and valence electrons. The binding and average kinetic energies of valence electrons are much smaller than the energy of the incident protons at large impact parameters and are similar among these polyatomic molecules.

ACKNOWLEDGMENTS

The authors would like to thank M. Hoffmann and O. Döhr for operation of the PTB ion accelerators and A. Pausewang and W. Helms for the technical support. This work was carried out within the EMRP Joint Research Project "BioQuaRT". The EMRP is jointly funded by the EMRP participating countries within EURAMET and the European Union. P.d.V. acknowledges financial support from the European Union's FP7-People Program (Marie Curie Actions) within the Initial Training Network No. 608163 "ARGENT".

APPENDIX

The number of secondary electrons $\dot{N}_s$ emitted per unit time from a length L of an ionizing particle beam trajectory into the solid angle $\Delta\Omega$ located at angle θ with respect to the beam direction in the energy range W to $W + \Delta W$ is given by [3]

$$\dot{N}_s(W,\theta) = \dot{N}_p \rho_t L \frac{d^2\sigma_{\rm ion}}{dW d\Omega}(W,\theta)\Delta W \Delta\Omega, \tag{A1}$$

where $\dot{N}_p$ is the number of primary particles per time passing a cross-sectional area of the molecular beam and ρ_t is the number of the target particles per volume (number density). The quantity $d^2\sigma_{\rm ion}/dWd\Omega$ is the double-differential cross section (DDCS) for ionization of target molecules by the primary particles, which has dimensions of area per energy and per solid angle.

In the experiments, the number density of target molecules within the gas jet is nonuniform, so that the rate of production of secondary electrons varies over the interaction zone where the primary particle beam and the target gas jet overlap. Electrons emitted from the interaction zone with an energy in the range W to $W + \Delta W$ into the solid angle $\Delta\Omega$ covered by the entrance aperture of the spectrometer which is located at angle θ with respect to the primary beam direction will be detected with a detection efficiency $\eta(W)$. The count rate of detected electrons originating from collisions of primary particles with gas jet molecules is given by

$$\dot{N}_{{\rm det},s}(W,\theta) = \dot{N}_p \dot{N}_g n_{g,p}(\theta)\eta(W) \times \frac{d^2\sigma_{\rm ion}}{dW d\Omega}(W,\theta)\Delta W \Delta\Omega, \tag{A2}$$

where $\dot{N}_g$ is the number of gas molecules emitted per unit time from the nozzle, $n_{g,p}(\theta)$ is the effective number of target molecules per area in the projectile-beam direction divided by the rate of target molecules ejected from the nozzle, and $\eta(W)$ is the detection efficiency of the spectrometer for electrons of energy W.

The rate of passing primary particles $\dot{N}_p$ can be obtained from the beam current I_{FC} measured with the Faraday cup as follows:

$$\dot{N}_p = \frac{I_{FC}}{qek_I}, \tag{A3}$$

where q and e are the charge number of the primary particles and the elementary charge, respectively. The quantity k_I is the collection efficiency of the Faraday cup.

The rate of gas molecules emitted from the nozzle can be related to the pressure p_g measured by the ion gauge in the spectrometer vacuum chamber in the presence of the gas jet via the ideal gas law

$$\dot{N}_g = \frac{p_g \dot{V}_{TMP}}{k_B T_g} k_p^{(g)} k_V^{(g)}, \tag{A4}$$

where $\dot{V}_{TMP}$ is the nominal pumping speed of the turbomolecular pump, k_B is the Boltzmann constant, and T_g is the gas temperature, which is assumed to be equal to the room temperature. As gas pressure measurement and pumping speed depend on the gas type, gas-dependent correction factors $k_p^{(g)}$ and $k_V^{(g)}$ have to be applied to the ion gauge reading and the pumping speed.

Inserting Eqs. (A3) and (A4) into Eq. (A2) and taking into account that the spectrometer also detects a background of electrons produced from processes other than interactions between the gas jet and the primary particle beam with a current $I_p^{(g)}$ give, for the count rate $\dot{N}_{\rm det}^{(g)}(W,\theta)$ of electrons for a measurement at scattering angle θ,

$$\dot{N}_{\rm det}^{(g)}(W,\theta) = \left(\frac{\dot{V}_{TMP}}{qek_Ik_B} I_p^{(g)} \frac{p_g}{T_g} k_p^{(g)} k_V^{(g)} n_{g,p}(\theta)\eta(W) \times \frac{d^2\sigma_{\rm ion}}{dWd\Omega}(W,\theta)\Delta W \Delta\Omega\right) + \frac{I_p^{(g)}}{qek_I}\beta(W)\eta(W), \tag{A5}$$

where $\beta(W)$ is the number of background electrons per incident primary particle that enters the spectrometer aperture within the angular range of acceptance. When the gas jet is turned off, the corresponding measurement equation for the count rate is

$$\dot{N}_{\rm det}^{(b)}(W,\theta) = \frac{I_p^{(b)}}{qek_I}\beta(W)\eta(W), \tag{A6}$$

where $\dot{N}_{\rm det}^{(b)}(W,\theta)$ is the background count rate and $I_p^{(b)}$ is the beam current in the background measurements.

It is convenient to rewrite Eq. (A5) in the following form:

$$\dot{N}_{\rm det}^{(g)}(W,\theta) = \left(C I_p^{(g)} \frac{p_g}{T_g} k_p^{(g)} k_V^{(g)} n_{g,p}(\theta)\eta(W) \times \frac{d^2\sigma_{\rm ion}}{dWd\Omega}(W,\theta)\Delta W \Delta\Omega\right) + I_p^{(g)} \frac{\dot{N}_{\rm det}^{(b)}(W,\theta)}{I_p^{(b)}}, \tag{A7}$$

where C is a constant during our measurements and is independent of the primary particle (protons or electrons) and gas type (argon or THF):

$$C = \frac{\dot{V}_{TMP}}{qek_Ik_B}. \tag{A8}$$

[1] M. E. Rudd, Y. K. Kim, D. H. Madison, and J. W. Gallagher, Rev. Mod. Phys. **57**, 965 (1985).

[2] M. E. Rudd, Y. K. Kim, D. H. Madison, and T. J. Gay, Rev. Mod. Phys. **64**, 441 (1992).

[3] M. Rudd, Y. Kim, T. Märk, J. Schou, N. Stolterfoht, and L. Toburen, *Secondary Electron Spectra from Charged Particle Interactions*, ICRU Report No. 55 (International Commission on Radiation Units and Measurements, Bethesda, MD, 1996).

[4] N. Stolterfoht, R. D. DuBois, and R. D. Rivarola, *Electron Emission in Heavy Ion-Atom Collisions*, Springer Series on Atomic, Optical, and Plasma Physics Vol. 20 (Springer, Berlin, 1997).

[5] M. Schultz and D. H. Madison, Int. J. Mod. Phys. A **21**, 3649 (2006).

[6] M. Schulz, R. Moshammer, D. Fischer, H. Kollmus, D. H. Madison, S. Jones, and J. Ullrich, Nature (London) **422**, 48 (2003).

[7] D. Madison, M. Schulz, S. Jones, M. Foster, R. Moshammer, and J. Ullrich, J. Phys. B **35**, 3297 (2002).

[8] A. Hasan, N. V. Maydanyuk, B. Fendler, A. Voitkiv, B. Najjari, and M. Schulz, J. Phys. B **37**, 1923 (2004).

[9] A. Hasan, T. Arthanayaka, B. R. Lamichhane, S. Sharma, S. Gurung, J. Remolina, S. Akula, D. H. Madison, M. F. Ciappina, R. D. Rivarola, and M. Schulz, J. Phys. B **49**, 04LT01 (2016).

[10] B. Boudaïffa, P. Cloutier, D. Hunting, M. A. Huels, and L. Sanche, Science **287**, 1658 (2000).

[11] B. Rudek, A. Arndt, D. Bennett, M. Wang, and H. Rabus, Eur. Phys. J. D **69**, 237 (2015).

[12] L. H. Toburen and W. E. Wilson, J. Chem. Phys. **66**, 5202 (1977).

[13] M. E. Rudd, T. V. Goffe, R. D. DuBois, and L. H. Toburen, Phys. Rev. A **31**, 492 (1985).

[14] M. A. Bolorizadeh and M. E. Rudd, Phys. Rev. A **33**, 888 (1986).

[15] F. Gobet, S. Eden, B. Coupier, J. Tabet, B. Farizon, M. Farizon, M. J. Gaillard, M. Carré, S. Ouaskit, T. D. Märk, and P. Scheier, Phys. Rev. A **70**, 062716 (2004).

[16] L. Fernández-Menchero and S. Otranto, J. Phys. B **47**, 035205 (2014).

[17] C. Champion and C. Dal Cappello, Nucl. Instrum. Methods Phys. Res., Sect. B **267**, 881 (2009).

[18] O. Boudrioua, C. Champion, C. Dal Cappello, and Y. V. Popov, Phys. Rev. A **75**, 022720 (2007).

[19] J. Tabet, S. Eden, S. Feil, H. Abdoul-Carime, B. Farizon, M. Farizon, S. Ouaskit, and T. D. Märk, Phys. Rev. A **82**, 022703 (2010).

[20] Y. Iriki, Y. Kikuchi, M. Imai, and A. Itoh, Phys. Rev. A **84**, 032704 (2011).

[21] Y. Iriki, Y. Kikuchi, M. Imai, and A. Itoh, Phys. Rev. A **84**, 052719 (2011).

[22] A. Itoh, Y. Iriki, M. Imai, C. Champion, and R. D. Rivarola, Phys. Rev. A **88**, 052711 (2013).

[23] C. Champion, H. Lekadir, M. E. Galassi, O. Fojón, R. D. Rivarola, and J. Hanssen, Phys. Med. Biol. **55**, 6053 (2010).

[24] P. de Vera, R. Garcia-Molina, I. Abril, and A. V. Solov'yov, Phys. Rev. Lett. **110**, 148104 (2013).

[25] P. de Vera, R. Garcia-Molina, and I. Abril, Phys. Rev. Lett. **114**, 018101 (2015).

[26] R. Dörner, V. Mergel, O. Jagutzki, L. Spielberger, J. Ullrich, R. Moshammer, and H. Schmidt-Böcking, Phys. Rep. **330**, 95 (2000).

[27] J. Ullrich, R. Moshammer, A. Dorn, R. Dörner, L. P. H. Schmidt, and H. Schmidt-Böcking, Rep. Prog. Phys. **66**, 1463 (2003).

[28] R. R. Wilson, Radiology **47**, 487 (1946).
[29] J. S. Loeffler and M. Durante, Nat. Rev. Clin. Oncol. **10**, 411 (2013).
[30] D. Schardt, T. Elsässer, and D. Schulz-Ertner, Rev. Mod. Phys. **82**, 383 (2010).
[31] H. Brede, M. Cosack, G. Dietze, H. Gumpert, S. Guldbakke, R. Jahr, M. Kutscha, D. Schlegel-Bickmann, and H. Schölermann, Nucl. Instrum. Methods **169**, 349 (1980).
[32] R. Böttger, Physikalisch-Technische Bundesanstalt Report No. PTB-6.41-02-2, 2002 (unpublished).
[33] A. H. Firester, Rev. Sci. Instrum. **37**, 1264 (1966).
[34] D. P. Seccombe, S. A. Collins, and T. J. Reddish, Rev. Sci. Instrum. **72**, 2550 (2001).
[35] W. Y. Baek, M. Bug, H. Rabus, E. Gargioni, and B. Grosswendt, Phys. Rev. A **86**, 032702 (2012).
[36] E. M. Purcell, Phys. Rev. **54**, 818 (1938).
[37] P. Dahl, M. Rodbro, B. Fastrup, and M. E. Rudd, J. Phys. B **9**, 1567 (1976).
[38] M. O. Krause and J. H. Oliver, J. Phys. Chem. Ref. Data **8**, 329 (1979).
[39] W. Mehlhorn and D. Stalherm, Z. Phys. **217**, 294 (1968).
[40] A. Jablonski, F. Salvat, and C. J. Powell, *NIST Electron Elastic-Scattering Cross-Section Database*, 3rd ed. (NIST, Gaithersburg, MD, 2010).
[41] E. Grusell, U. Isacsson, A. Montelius, and J. Medin, Phys. Med. Biol. **40**, 1831 (1995).
[42] M. U. Bug, Ph.D. thesis, University of Wollongong, 2014.
[43] M. Rudd, L. Toburen, and N. Stolterfoht, At. Data Nucl. Data Tables **23**, 405 (1979).
[44] M. E. Rudd, Phys. Rev. A **44**, 1644 (1991).
[45] M. Bernal and J. Liendo, Nucl. Instrum. Methods Phys. Res., Sect. B **251**, 171 (2006).
[46] J. P. Hansen and L. Kocbach, J. Phys. B **22**, L71 (1989).
[47] J. Lindhard, K. Dan. Vidensk. Selsk. Mat. Fys. Medd **28**, 1 (1954).
[48] R. H. Ritchie, Phys. Rev. **106**, 874 (1957).
[49] W. Brandt and M. Kitagawa, Phys. Rev. B **25**, 5631 (1982).
[50] A. Salin, J. Phys. B **2**, 631 (1969).
[51] M. Dingfelder, Radiat. Prot. Dosim. **99**, 23 (2002).
[52] I. Abril, R. Garcia-Molina, P. de Vera, I. Kyriakou, and D. Emfietzoglou, Adv. Quantum Chem. **65**, 129 (2013).
[53] R. Garcia-Molina, I. Abril, I. D. Kyriakou, and D. Emfietzoglou, in *Radiation Damage in Biomolecular Systems*, edited by G. García Gómez-Tejedor and M. C. Fuss (Springer, Dordrecht, 2012), Chap. 15, pp. 239–261.
[54] S. Heredia-Avalos, R. Garcia-Molina, J. M. Fernández-Varea, and I. Abril, Phys. Rev. A **72**, 052902 (2005).
[55] Z. Tan, Y. Xia, M. Zhao, X. Liu, F. Li, B. Huang, and Y. Ji, Nucl. Instrum. Methods Phys. Res., Sect. B **222**, 27 (2004).
[56] M. W. Schmidt, K. K. Baldridge, J. A. Boatz, S. T. Elbert, M. S. Gordon, J. H. Jensen, S. Koseki, N. Matsunaga, K. A. Nguyen, S. Su, T. L. Windus, M. Dupuis, and J. A. Montgomery, J. Comput. Chem. **14**, 1347 (1993).
[57] B. Bransden and C. Joachain, *Physics of Atoms and Molecules* (Longman, London, 1983).
[58] W. E. Wilson and L. H. Toburen, Phys. Rev. A **11**, 1303 (1975).
[59] L. H. Toburen and W. E. Wilson, Phys. Rev. A **5**, 247 (1972).
[60] D. J. Lynch, L. H. Toburen, and W. E. Wilson, J. Chem. Phys. **64**, 2616 (1976).